NASA/TM—2017-219504/REV1

Rotational Raman-Based Temperature Measurements in a High-Velocity Turbulent Jet

Randy J. Locke
Vantage Partners, LLC, Brook Park, Ohio

Mark P. Wernet and Robert C. Anderson
Glenn Research Center, Cleveland, Ohio

This Revised Copy, numbered as NASA/TM—2017-219504/REV1, December 2017, supersedes the previous version, NASA/TM—2017-219504, June 2017, in its entirety.

December 2017

NASA STI Program . . . in Profile

Since its founding, NASA has been dedicated to the advancement of aeronautics and space science. The NASA Scientific and Technical Information (STI) Program plays a key part in helping NASA maintain this important role.

The NASA STI Program operates under the auspices of the Agency Chief Information Officer. It collects, organizes, provides for archiving, and disseminates NASA's STI. The NASA STI Program provides access to the NASA Technical Report Server—Registered (NTRS Reg) and NASA Technical Report Server—Public (NTRS) thus providing one of the largest collections of aeronautical and space science STI in the world. Results are published in both non-NASA channels and by NASA in the NASA STI Report Series, which includes the following report types:

- TECHNICAL PUBLICATION. Reports of completed research or a major significant phase of research that present the results of NASA programs and include extensive data or theoretical analysis. Includes compilations of significant scientific and technical data and information deemed to be of continuing reference value. NASA counter-part of peer-reviewed formal professional papers, but has less stringent limitations on manuscript length and extent of graphic presentations.

- TECHNICAL MEMORANDUM. Scientific and technical findings that are preliminary or of specialized interest, e.g., "quick-release" reports, working papers, and bibliographies that contain minimal annotation. Does not contain extensive analysis.

- CONTRACTOR REPORT. Scientific and technical findings by NASA-sponsored contractors and grantees.

- CONFERENCE PUBLICATION. Collected papers from scientific and technical conferences, symposia, seminars, or other meetings sponsored or co-sponsored by NASA.

- SPECIAL PUBLICATION. Scientific, technical, or historical information from NASA programs, projects, and missions, often concerned with subjects having substantial public interest.

- TECHNICAL TRANSLATION. English-language translations of foreign scientific and technical material pertinent to NASA's mission.

For more information about the NASA STI program, see the following:

- Access the NASA STI program home page at http://www.sti.nasa.gov

- E-mail your question to help@sti.nasa.gov

- Fax your question to the NASA STI Information Desk at 757-864-6500

- Telephone the NASA STI Information Desk at 757-864-9658

- Write to:
  NASA STI Program
  Mail Stop 148
  NASA Langley Research Center
  Hampton, VA 23681-2199

NASA/TM—2017-219504/REV1

Rotational Raman-Based Temperature Measurements in a High-Velocity Turbulent Jet

Randy J. Locke
Vantage Partners, LLC, Brook Park, Ohio

Mark P. Wernet and Robert C. Anderson
Glenn Research Center, Cleveland, Ohio

This Revised Copy, numbered as NASA/TM—2017-219504/REV1, December 2017, supersedes the previous version, NASA/TM—2017-219504, June 2017, in its entirety.

National Aeronautics and
Space Administration

Glenn Research Center
Cleveland, Ohio 44135

December 2017

Acknowledgments

This work was supported by the Turbulent Heat Transfer project under the Revolutionary Computational Aerosciences (RCA) program. The Authors would also like to recognize Garret Clayo for his assistance in the design and fabrication of the optical mounting system.

Revised Copy

This Revised Copy, numbered as NASA/TM—2017-219504/REV1, December 2017, supersedes the previous version, NASA/TM—2017-219504, June 2017, in its entirety.

After further work on the project, some items require revisions.

This work was sponsored by the
Transformative Aeronautics Concepts Program.

Level of Review: This material has been technically reviewed by technical management.

Available from

NASA STI Program
Mail Stop 148
NASA Langley Research Center
Hampton, VA 23681-2199

National Technical Information Service
5285 Port Royal Road
Springfield, VA 22161
703-605-6000

This report is available in electronic form at http://www.sti.nasa.gov/ and http://ntrs.nasa.gov/

Rotational Raman-Based Temperature Measurements in a High-Velocity, Turbulent Jet

Randy J. Locke
Vantage Partners, LLC
Brook Park, Ohio 44142

Mark P. Wernet and Robert C. Anderson
National Aeronautics and Space Administration
Glenn Research Center
Cleveland, Ohio 44135

Abstract

Spontaneous rotational Raman scattering spectroscopy is used to acquire the first ever high quality, spatially-resolved measurements of the mean and root mean square (rms) temperature fluctuations in turbulent, high-velocity heated jets. Raman spectra in air were obtained across a matrix of radial and axial locations downstream from a 50 mm diameter nozzle operating from subsonic to supersonic conditions over a wide range of temperatures and Mach numbers, in accordance with the Tanna matrix frequently used in jet noise studies. These data were acquired in the hostile, high noise (115 dB) environment of a large scale open air test facility at NASA Glenn Research Center (GRC). Temperature estimates were determined by performing nonlinear least squares fitting of the single shot spectra to the theoretical rotational Stokes spectra of N_2 and O_2, using a custom in-house code developed specifically for this investigation. The laser employed in this study was a high energy, long-pulsed, frequency doubled Nd:YAG laser. One thousand single-shot spectra were acquired at each spatial coordinate. Mean temperature and rms temperature variations were calculated at each measurement location. Excellent agreement between the averaged and single-shot temperatures was observed with an accuracy better than 2.5 percent for temperature, and rms variations in temperature between ±2.2 percent at 296 K and ±4.5 percent at 850 K. The results of this and planned follow-on studies will support NASA GRC's development of physics-based jet noise prediction, turbulence modeling and aeroacoustic source modeling codes.

The data set of Raman mean and rms temperature measurements covering the complete test matrix listed in Table 1 is available in an accompanying DVD (available online from www.sti.nasa.gov) for anyone interested in further analysis.

Nomenclature

B	Rotational constant for the vibrational state
c	Speed of light [m/s]
C	Scattering system constant
D_j	Nozzle diameter [mm]
g	Degeneracy of the state
h	Planck's constant [m^2kg/s]
I_{rot}	Intensity of an individual pure rotational line
I_o	Incident laser beam Intensity
J	Rotational Quantum number
k	Boltzmann constant [m^2kg/s^2K]
$\dot{m}$	mass flow [lb/s]

M	Mach number
Ma	Acoustic Mach number
N	Total number density [m^{-3}]
Q_{rot}	Partition function
Pr	Prandtl number
r	Radial coordinate [mm]
T’	rms temperature [K]
T_j	Temperature at jet exit [K]
T_∞	Ambient temperature [K]
ΔT	Difference between jet exit temperature and ambient temperature [K]
u’	rms in axial velocity component [m/s]
U_j	Axial velocity component at jet exit [m/s]
U_∞	Ambient velocity [m/s]
x	Axial coordinate [mm]
ϵ	Particle energy [eV]
ν_o	Pump laser wavenumber [cm^{-1}]
ν_{rot}	Scattered Raman wavenumber for the rotational line [cm^{-1}]
ΔE	Change in Energy
σ_{RE}	Error in the Raman temperature estimate [K]
σ_{TI}	Normalized rms variations in temperature of the flow [K]
σ_m	Measured variation in flow temperature [K]

Abbreviations:

AAPL	AeroAcoustic Propulsion Lab
GRC	Glenn Research Center
NPR	Ratio of the stagnation pressure of the jet to the ambient pressure
NTR	Ratio of the stagnation temperature of the jet to the ambient temperature
rms	Root Mean Square
SHJAR	Small Hot Jet Acoustic Rig

Introduction

Since the first reported measurement by Laurence (Ref. 1) in 1954, researchers have been studying high velocity turbulent jets in order to better understand the fluid dynamics of these flows. Even after all the years of study, much is left unknown primarily due to the difficulties encountered when trying to measure flow parameters, particularly temperature, in heated jets from subsonic to supersonic velocities. Traditional measurement techniques, (pressure transducers and resistance wires), and specifically those for temperature (thermocouples and hotwire anemometry), do not avail themselves satisfactorily to the conditions encountered in these flows, namely high temperature and high velocities. They are either severely restricted in temporal response, suffer from limited spatial resolution, or have a limited lifespan once in contact with the flows. Add to this the fact that they are intrusive to the flow and as such disturb and alter the very phenomenon that they are attempting to evaluate. Include the requirement for an instantaneous measurement, now needed for code validation efforts to accurately describe these turbulent flows, and these traditional methods are effectively eliminated. Clearly nonintrusive methods are required to obtain measurements of the requisite flow parameters.

The development of new laser-based measurement techniques in the 1970s allowed the first ever nonintrusive measurements to be acquired in turbulent flows. Laser Doppler Velocimetry (LDV) was the first such measurement (Ref. 2) and significantly expanded the data to measurements at high speed and elevated temperature flows. Particle Image Velocimetry (PIV) was the next generational improvement in nonintrusive flow measurement (Ref. 3). Due to advances in dual-head laser technology and digital imaging capability, the implementation of PIV became the preferred flow measurement technique for flow visualization and velocity measurements. While nonintrusive velocity measurements, specifically PIV, made huge strides, temperature measurement techniques in these hostile conditions lagged far behind. Early optical methods used to probe flows for temperature included Rayleigh scattering spectroscopy, Coherent anti-Stokes Raman Spectroscopy (CARS), vibrational Raman, and laser-induced fluorescence (LIF). Rayleigh spectroscopy has been utilized in jet flow facilities to measure the flow parameters such as velocity, density and temperature (Refs. 4 and 5) however, while the velocity and density data are of good quality, the rms temperature data are of lower quality and were frequently contaminated by entrainment of particulates in the flow. The Rayleigh technique also requires a complex optical system setup and alignment, and is very sensitive to ambient light and flare light issues. CARS (Ref. 6) is another scattering technique that has also been applied to measure temperature in high-speed gases, however, these measurements have largely been restricted to obtaining an average temperature in these flows but not the quickly fluctuating temperatures in highly turbulent shear layers. Since it too suffers from similar problems that plague Rayleigh measurements, namely, a complex setup and alignment issues, CARS has seen few successful applications to large-scale facilities with hostile environments; rather, CARS has been mainly relegated to bench-top measurement (Ref. 7) or environmentally friendly venues. CARS also suffers from the fact that at lower temperatures, fewer higher vibrational energy levels are populated and hence the anti-Stokes lines do not begin to be useful until around 600 K. Transient Gradient Spectroscopy (TGS), a relatively new diagnostic tool, has also seen recent application to temperature measurement. While this technique has seen a recent success in temperature measurement within jet flows (Ref. 8), it too suffers from a complex optical setup requiring precise alignment of multiple laser beams and as such is not amenable to large scale, outdoor facilities. Vibrational Raman spectroscopy, is another inelastic scattering technique which has reported species and temperature measurements (Ref. 9) but since it depends upon taking the ratio of the Stokes and anti-Stokes lines in the spectrum, it is incapable of measuring temperature below 600 K at atmospheric pressure since few vibrational states are populated at lower temperatures. LIF has also been employed in the measurement of flow parameters including temperature fluctuations in combusting flow fields by capturing the LIF of the combustion intermediary hydroxyl (OH^-) species or byproduct nitric oxide (NO) (Ref. 10). However, acquiring fluctuating temperature measurements in high speed, non-combusting flow fields presents problems associated with the seeding of the flow (Ref. 11) which is often required to provide a fluorescent species. Additionally, LIF has an added degree of complexity in its application in that it typically requires a dye laser and subsequent frequency doubling to obtain the necessary ultraviolet (UV) wavelengths.

Hence, a comprehensive, high quality set of temperature data to complement the large database of LDV and PIV measurements has remained elusive in jet flows for over 50 years. Until now, all CFD modelling efforts had to assume the temperature profile of the flow and the magnitude of the temperature fluctuations in hot jets. The data presented herein will show the first ever high quality measurements of the mean and rms fluctuations in temperature in heated jets at subsonic and supersonic conditions.

Project Description

NASA's Turbulent Heat Transfer (THX) project under the Transformational Tools & Technologies program is currently focused on acquiring benchmark temperature and velocity data in turbulent shear layers for validation of turbulent model assumptions used in computation fluid dynamics (CFD) codes. Standard CFD turbulence models lack the ability to predict the observed increase in the growth rate of the mixing layer and the current datasets of fluctuating temperatures report large uncertainties in the

measurements. Therefore, it is desired to produce a dataset of rms temperatures with small error and high spatial resolution. To that end, a Consensus velocity data set, has already been acquired by PIV measurements and has supplied the jet flow field mean velocity and turbulence properties (Ref. 12). Still lacking in this effort are temperature measurements of these flows which are required to further validate the CFD models and improve their accuracy. The objective of the tests described herein are to collect mean and rms temperature measurements via rotationally resolved Raman spectroscopy across a precisely defined measurement grid in the plume of a convergent hot jet for validation of CFD and noise modeling since regions of high turbulence are assumed to be the regions of peak fluctuations in temperature. The data measurement grid was developed by using the PIV Consensus data acquired with the same experimental rig configuration used in this investigation.

Rotational Raman was selected as the diagnostic for this test due mostly to the limitations imposed by the other methods, in particular the severe effects of the test environment on the diagnostic systems. The AeroAcoustic Propulsion Laboratory (AAPL), the location at NASA GRC selected for this series of tests, possesses, by its very nature, a number of features that could hinder or completely preclude the performance of certain optical diagnostics. Several major considerations include: (1) The AAPL is open to the outside environment and as such experiences large temperature variations over the course of a day-long test, (2) High sonic noise levels upwards of 115 dB, (3) High ambient light levels due to the large 55 ft wide by 36 ft high exhaust-door which must remain open during tests, and (4) Inaccessibility by personnel during the tests. Temperatures in the AAPL during the testing period ranged from 4 °C in the morning to 21 °C in the afternoon. For diagnostics that require a high degree of alignment this temperature shift could necessitate constant shutdown of the facility to enter the test venue to make alignment adjustments followed by a protracted ramp-up back to test conditions. Considering the time it takes to achieve test temperature condition, this was not a feasible option. The high sonic vibrations, common with near-sonic to super-sonic flows could also adversely affect these alignment sensitive methods. High light levels in the AAPL can also play a limiting role in the success of a diagnostic, Researchers conducting Rayleigh experiments during an earlier campaign in the AAPL to obtain temperature and velocity measurements had to resort to extreme measures in an effort to eliminate ambient light.

Taking all of the above into consideration and based upon previous experimental experience in performing Raman in similar environment conditions, rotational Raman was selected as the diagnostic method for the measurement effort. Rotational Raman does suffer from some of the same disadvantages as the other considered diagnostics, among these is the fact that rotational Raman, like Rayleigh and CARS, is a point measurement and thus the data acquisition will be slow because of the large size of the measurement grid needed to gather a high spatial resolution temperature survey. It is also subject to the same data collection interferences caused by ambient light and by laser scatter from particulates or droplets entrained in the flow. Additionally, since the rotational Raman spectra is a relatively weak phenomenon, a large laser fluence is necessary to elicit the spectrum which could lead to laser-induced breakdown of the gas molecules in the air thereby obscuring or grossly interfering with the rotational spectrum. The advantages of rotational Raman however make-up for the shortfalls in the diagnostic. Rotational Raman is a well-established, nonintrusive diagnostic; it allows for instantaneous measurements, additionally, and unlike vibrational Raman, it is amenable to acquiring temperature measurements in a wide range of temperatures, including those of the proposed test. Also, with recent developments in long-pulsed lasers, the problems due to laser-induced breakdown can be solved by operating the laser at longer pulse widths which still supplies the requisite laser fluence in the focal volume to obtain the measurements, but with an extended pulse duration that avoids breakdown of the air. A final advantage to rotational Raman is that it is a relative simple experimental setup which does not need constant optical realigning, thereby allowing uninterrupted data acquisition in harsh environments of large scale facilities.

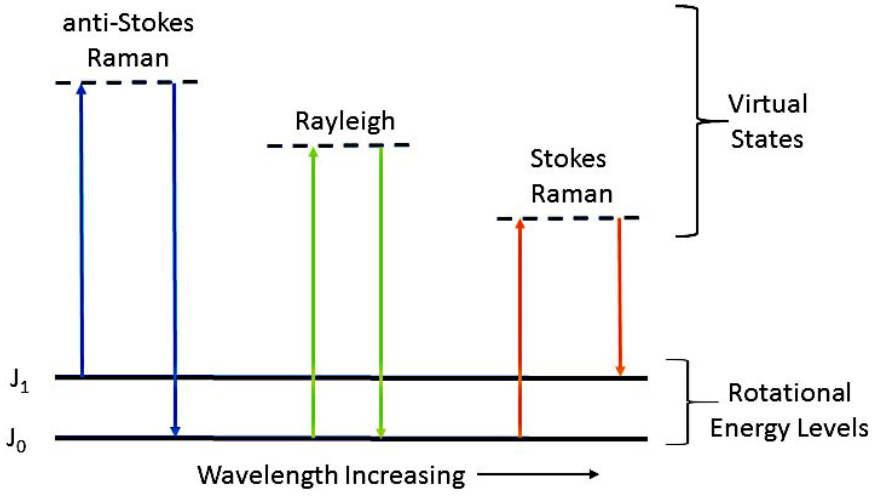

Figure 1.—Simplified energy diagram outlining the rotational Raman process.

Raman Scattering

Photons can interact with molecules in a number of different ways: they can be absorbed and re-emitted via fluorescence; they can be elastically scattered in a process called Rayleigh scattering; or they can be inelastically scattered through Raman scattering. The scattering process is shown schematically in Figure 1. For a thorough discourse on Raman spectroscopy theory and practices, the reader is directed to an excellent treatment by Ferraro and Nakamoto (Ref. 13). In general, Raman is an inelastic scattering process, with a signal intensity approximately 10^{-3} of that from Rayleigh. Raman scattering is not dependent on wavelength but is linear with respect to the species number density and is species specific by virtue of the quantization of individual molecular energy states.

The incident or colliding photon can impart energy to the molecule equivalent to the energy necessary to elevate the molecule to the next energy level (in our case rotational) causing the photon to scatter at a lower frequency, called Stokes scattering. Conversely, during the collision the photon can remove from the molecule the same amount of energy and be scattered at a higher frequency, called anti-Stokes scattering. At constant pressure, the amplitude of the Raman signal will scale as T^{-1} reflecting the decrease in density with increasing temperature.

The rotational states of the target molecule are spread over a number of discrete energy levels. For each of these states there is a certain probability of being populated by the molecule when the system is in thermal equilibrium. This probability distribution is given by Boltzmann (Ref. 14):

$$N_j = N \frac{g_j \exp\left(-\frac{\epsilon_j}{kT}\right)}{\sum_j g_j \exp\left(-\frac{\epsilon_j}{kT}\right)} \tag{1}$$

Where N_j is the particle number density in the jth state of energy ϵ; N is the total number density; k is Boltzmann's constant; T is the temperature; and g_j is the degeneracy of the state. The rotational population distribution is given by the following:

$$N_J = \frac{N}{Q_{rot}} g_I (2J+1) \exp\left(-\frac{hcBJ(J+1)}{kT}\right) \tag{2}$$

where g_I is the statistical weight factor dependent on coupling with the spin of the nucleus. The temperature dependence of the population distribution is illustrated in Figure 2 where, for clarity, only the odd numbered J-states for nitrogen are shown.

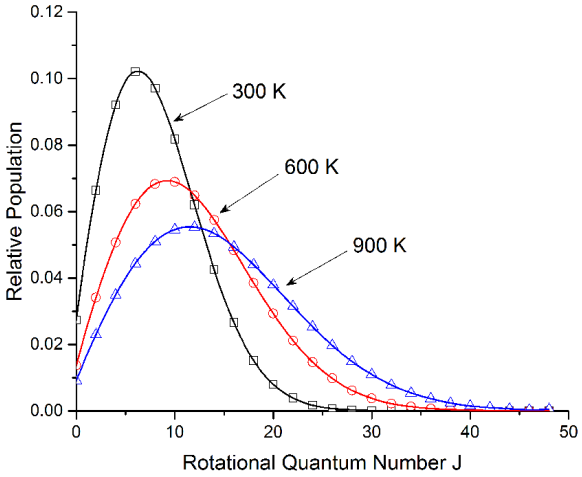

Figure 2.—Plot showing the temperature dependence and relative population distribution of rotational levels at three different temperatures for the odd numbered *J*-states for nitrogen.

Calibration Laboratory Setup

In order to demonstrate the rotational Raman measurement technique and to also to establish the accuracy of the diagnostic in a well characterized environment, the experiment was first performed on an optical table in a laboratory (Figure 3) which closely matched the experimental layout planned in the actual facility. The output from a long-pulsed, 10 Hz Agilite Nd:YAG laser from Continuum was tuned to a 500 nsec pulse width at 600 mJ/pulse. The 9 mm diameter output beam was focused by a 500 mm spherical lens to a roughly 70 μm spot 5 mm downstream from the exit plane of a programmable electric heat gun (Stienell model HG-2310-LCD) with a nominal tuning range of 296 to 922 K. The 20 mm diameter heat gun exit orifice was fitted with a condenser nozzle to reduce the exit diameter of the flow down to 10 mm. The rotational Raman scattering elicited in the heat gun's flow was collected by two matched f/1.4, 85 mm Nikon lens set at a 4.0 f-stop. The lenses were vertically mounted and focused on the laser focal volume approximately 530 mm distant. Each lens was displaced from the horizontal plane and tilted by 6° (upper –6°, lower +6°). The measurement volume is defined by the intersection of the laser beam diameter and the two 85 mm lens collection cones. The length of the 70 micron diameter laser beam collected by the 85 mm lenses is defined by the size of the fiber bundle used to collect and transmit the light to the spectrometer. The entrance face of the fiber bundles are 1.1 mm in diameter. The 85 mm lenses image a 6 mm length of the laser beam onto the face of the fiber bundle. The resulting cylindrical probe volume is 4.3×10^{-3} mm^3.

The light captured by each lens was passed through a 532 nm RazorEdge long-pass 25.4 mm filter attached to the rear of each camera lens mount. The filtered light was focused onto a bifurcated fiber bundle from Fiberoptic Systems, Inc. The input ends of the bifurcated fiber bundle each contained 57 100 μm diameter fibers which were formed into a linear array at the output end of the bundle. The linear fiber bundle output was coupled to the entrance slit of an Acton 500 mm imaging spectrometer with an 1800 gr ruled grating and a wavelength centerline of 537 nm resulting in a spectral wavelength span of approximately 12 nm. Since the 100 μm fibers of the transmission bundle were arranged linearly at the slit, the slit of the spectrometer was opened to its maximum of 2 mm allowing the fibers to act as their own 100 μm slit. A PI-MAX2 ICCD camera with 18 mm gated intensifier from Princeton Instruments was coupled to the exit of the spectrometer and the resultant rotational Raman spectra captured using Princeton's WinSpec32 software. To verify alignment of the 532 nm laser pulse, the thermocouple and the two camera lenses, a 635 nm diode laser was fiber-coupled to the rear of the two 85 mm collection lenses and directed back to the probe volume, where the alignment of all three components of the measurement system could be visually confirmed by the intersection of the back projected/focused diode laser beams.

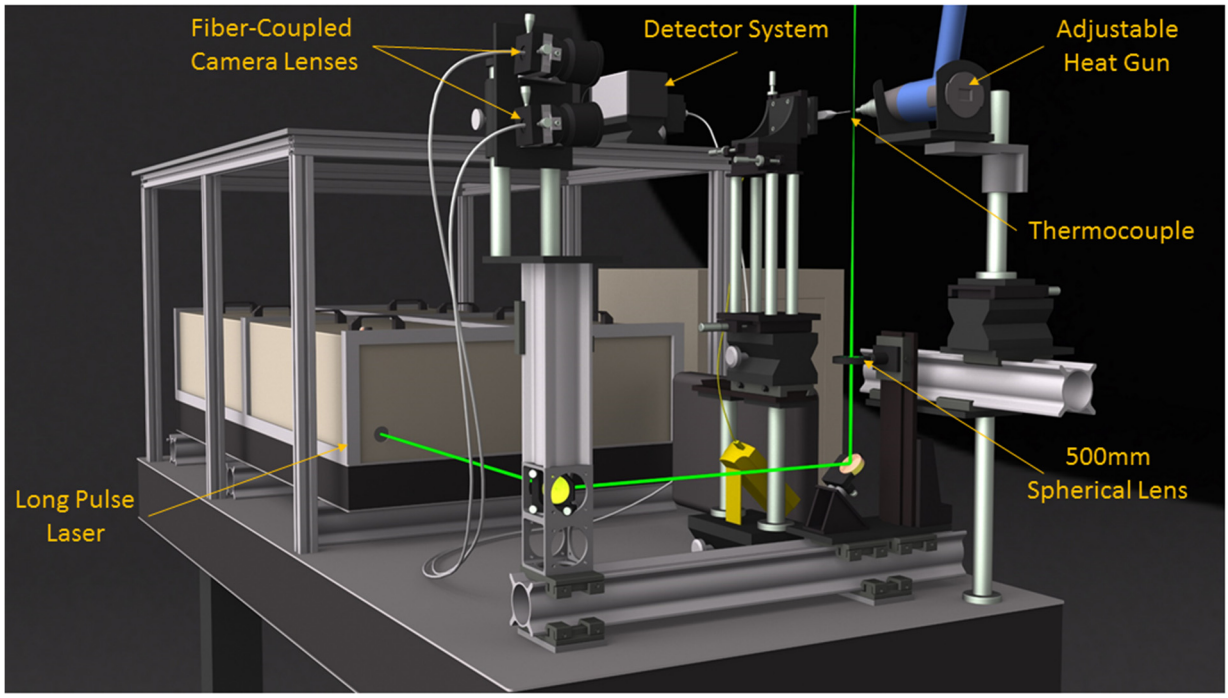

Figure 3.—Schematic of the rotational Raman for temperature calibration experimental setup.

For each temperature measurement point in the optical table set-up, the heat gun's setting was verified at the same location of the Raman focal volume in the flow by using a 0.025 in. diameter sheathed thermocouple from Omega. The thermocouple provided the mean flow temperature. Once the desired temperature was reached and stabilized, the thermocouple was withdrawn from the flow and the Raman data acquisition sequence was initiated. Each data set contained 1000 single shots, acquired at the laser rep rate of 10 Hz. The calibration was performed at thirteen temperatures over a range of 296 to 840 K. In order to establish the rms temperature fluctuations in the heated flow exiting the heat gun, additional tests were performed using an unsheathed 0.0005 in., Omega (CHAL-0005), K-Type thermocouple, with a frequency response of approximately 500 Hz. The CHAL-0005 Thermocouple was mounted in a ceramic mount in order to support it when placed in the heat gun's flow. The thermocouple was again placed in the same location as the Raman temperature measurement and the signal from the thermocouple was collected and digitized at 1 kHz. First the baseline error in the thermocouple was established by measuring the temperature of the ambient air, which showed an error of ±0.15 K. Next the thermocouple was used to measure the heat gun flow over the range of 296 to 840 K, where the time records showed a periodic rising and falling of the temperature in the heat gun flow caused by the heating element cycling on/off in order to hold the required setpoint temperature. The heat gun operates with a ±10 K control band, yielding an rms temperature of ±5 K. Hence, any temperature measurements in the heat gun flow will exhibit an rms fluctuation of at least ±5 K. The rms temperature measured using the 0.0005 in. thermocouple were nearly constant across the entire 296 to 840 K measurement range, confirming that the heat gun was providing a nominally isothermal environment for the calibration measurements.

Data Processing

To extract temperature from the rotational Raman spectra, an iterative process was developed which determines the best fit between the measured spectrum and the spectrum computed using a pure-rotational Raman scattering model based on software created under a NASA contract by Aerodyne Research. To model the Raman scattering spectrum an assumption is first made that the gas composition is a mixture of

only molecular nitrogen and oxygen. This can be done since the measurements are to be made in air and other atmospheric gaseous components do not contribute significantly to the Raman signal. For a given temperature, the model computes Raman line locations and strengths in the Raman Stokes (S) bands of nitrogen and oxygen. Rotational quantum numbers used range from 0 to 50. The merged array of Raman lines for N_2 and O_2 with their respective strengths and wavenumbers, is then convolved with a Voigt kernel derived from the spectral profile of the pump laser wavelength peak as measured through the optical system.

In rotational Raman scattering, an incident photon of energy v_0, interacts with a molecule such that the molecule may absorb part of the energy of this photon and be promoted to a higher rotational level. The difference, ΔE, in the rotational energy levels results in a scattered photon reduced in energy ($v_0 - \Delta E$). The intensity of an individual pure rotational line of the S-branch in the Raman scattering spectrum may be computed (Ref. 15) using:

$$I_{\text{rot}} = C\, I_0\, N \left(v_0 - v_{\text{rot}}\right)^4 \frac{3(J+1)(J+2)(2J+1)}{2(2J+3)(2J+1)}\, e^{\left[-\frac{J(J+1)hc\,B}{kT}\right]} \tag{3}$$

where N is the density of molecules of interest, v_0 is the pump laser wavenumber, v_{rot} is the scattered Raman wavenumber for the rotational line, J is the rotational quantum number, h is Plank's constant, c is the speed of light, B is the rotational constant for the vibrational state, k is the Boltzmann constant, T is the absolute temperature, and I_0 is the laser intensity. The scattering system constant C, assumed independent of J, contains those parameters that are constants for a fixed scattering system (Refs. 16 to 18). These include the relative Raman cross-section, nuclear spin weight, and vibrational-rotational interaction term (Ref. 19).

Examples of the model output are shown in Figure 4(a) where a stick spectrum of the rotational Raman peak intensities at 837 K is shown and in Figure 4(b) where the convolved model output at 837 K is shown. It should be noted that when there is an overlap of N_2 and O_2 peaks in the stick spectrum, the resultant convolved spectrum will show some abnormally intense peaks due to that overlap.

In the data processing stage, the 1000 single-shot spectra were read into the Matlab based data reduction software. In each acquisition sequence, there were typically several bad spectra due to the wait time of the camera/spectrometer/image intensifier. Additionally, there were times when particulates in the flow passed through the measurement volume producing strong signals at the laser line wavelength, which were strong enough to yield Rayleigh/laser line peaks of higher intensity than the Raman signal. In order to remove these spurious spectra, the data set was sorted to remove the 10 highest amplitude spectra, hence only 990 single shot spectra were used in each ensemble.

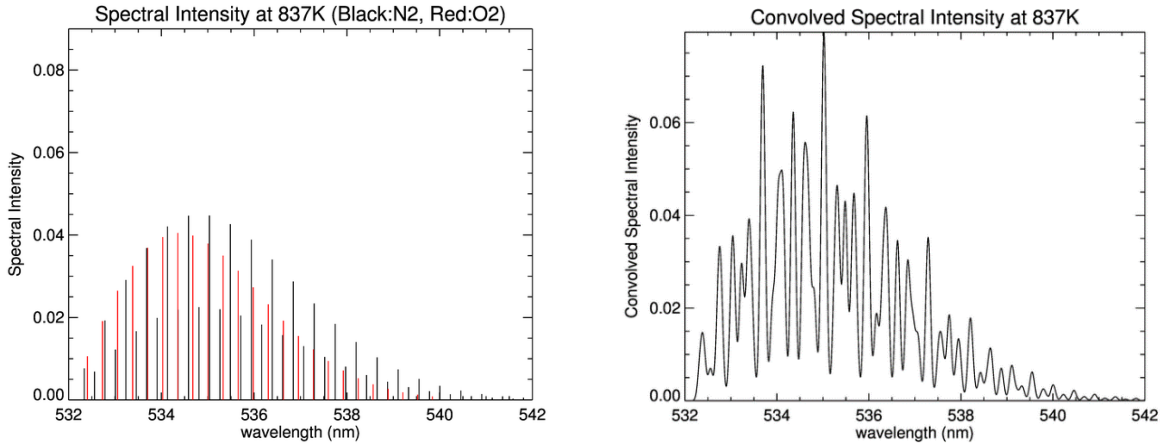

Figure 4.—(a) Rotational Raman stick spectrum of molecular oxygen and nitrogen at 837 K. (b) Convolved rotational Raman spectrum of O_2 and N_2.

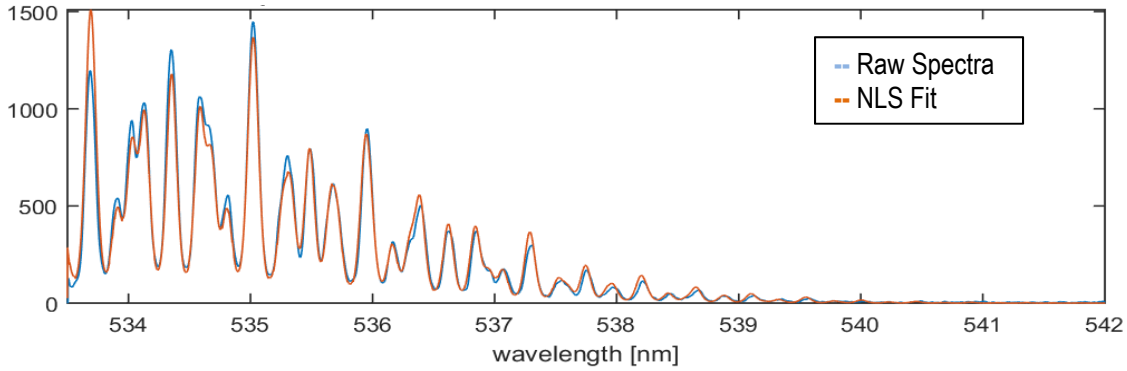

Figure 5.—Sample averaged rotational Raman temperature spectrum with fit for T_{cal} = 547 K. The spectrum is elongated in the x-axis to show detail.

The 990 spectra were then used to compute an average spectra, which was fit to the model function described previously using a nonlinear least squares routine. The model parameters used in the fit included the temperature, the Raman signal amplitude, the kernel width (instrument function) and the spectrometer grating calibration parameters, which included the laser line center location. The fit of the mean spectra provided the initial estimates for all of the single shot spectral fits. The estimated temperatures from the processed spectra were then used to compute the mean temperature estimate and the rms temperature across the ensemble, T'. The time to process the 990 spectra was on the order of 1 min on a 20 core based CPU.

For an optimally designed and configured experiment, the instrument function is very narrow and the model function remains on the baseline across the entire spectra, just like the Raman spectral line stick strengths shown in Figure 4(a). However, there is always some finite width to the instrument function, which results in the individual lines interacting and the build-up of a pedestal in the peak region of the Raman spectra, which lifts the spectra off of the baseline. The development of the baseline is fully accounted for in the model function as the instrument function broadens during the fitting process. A sample averaged spectrum acquired at 547 K with the calibration setup and its corresponding fit are shown in Figure 5.

A Voigt profile was used to model the instrument function since this most closely resembled the Rayleigh line profiles acquired prior to each run day. The Voigt profile function had two input parameters, the Gaussian width and the Lorentzian width. The Lorentzian width controlled the width of the kernel near the baseline and had the most influence on the interaction of the instrument function with adjoining lines in the spectra. Control of the Lorentzian width independent of the Gaussian peak width enabled the model function to build a pedestal that matched the data lift off from the axis, yet retained good fidelity in the overlapping N_2/O_2 spectral lines to yield sharply shaped peaks in the generated spectral model.

Calibration Results

The Raman spectra acquired at the 13 different temperature settings on the heat gun were processed according to the procedures described in the preceding data reduction discussion. The ensemble of 990 measurements at each point are used to compute the mean and rms gas temperature. Figure 6, plots the mean temperature of all 990 accumulated spectra along with the rms error bars at each temperature. The mean calibration temperature measurements are found to be accurate to < 2.5 percent over the range of 296 to 850 K. Here accuracy is defined as the deviation of the measurement from the true (known) value. For these calibration measurements the mean temperature level is measured using a thermocouple. The reported error is the deviation of the Raman based mean temperature measurement from the thermocouple measurements.

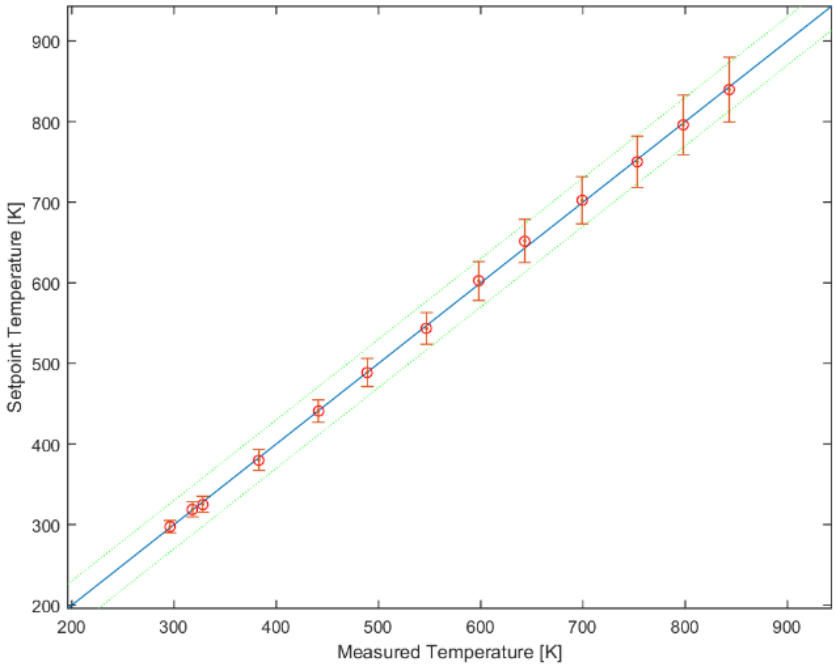

Figure 6.—Plot comparing the thermocouple reading versus the calculated Temperature and the RMS variations (plotted as error bars) in temperature over the range of calibration temperature range settings.

The Raman based calibration rms temperature estimate is ±2.2 percent at 296 K and ±4.5 percent at 850 K. The measured rms temperatures are higher than the rms levels measured using the 0.0005 in. thermocouple in the heat gun flow. The Raman temperature measurements reported here illustrate the best case measurement accuracy that can be expected using the Raman thermometry diagnostic. The calibration plot error bars in Figure 6 clearly delineate that there is a linear dependence on the measured rms temperature with increasing temperature. This is an inherent property of a molecular based scattering technique. The molecules in the probe volume can have any one of a number of states as defined by the Boltzmann distribution. The number of allowable states increases with temperature, hence the rms temperature increases with increasing temperature of the gas. A linear fit to the rms temperature as a function of the known temperature yields a relation for the expected error in the Raman based temperature diagnostic:

$$\sigma_{RE} = 0.057T - 11.92\,\mathrm{K} \tag{4}$$

This expression will be used later to predict the expected error resulting from the Raman temperature measurement technique when we examine the thermal fluctuation measurements in the heated jet flows. These measurement errors agree with those reported by others in the literature using molecular based scattering techniques for measuring temperature. In the work of Bolin (Ref. 20), CARS thermometry measurements were obtained in a calibrated oven in order to obtain mean temperature measurements at 300, 600, and 900 K. The processed data showed rms fluctuation levels of ±9, ±16, ±22 K respectively, across the temperature range.

AAPL Laboratory and Experimental Setup

All the data presented herein was obtained on the Small Hot Jet Acoustic Rig (SHJAR) located within the AeroAcoustic Propulsion Laboratory (AAPL) at NASA GRC. The SHJAR (Figure 7) is a single flow stream free jet rig capable of operating over a range of Mach numbers up to M2 at static temperature ratios up to 2.8. The AAPL (Figure 8) is a 19.8 m radius geodesic dome with its interior walls covered by

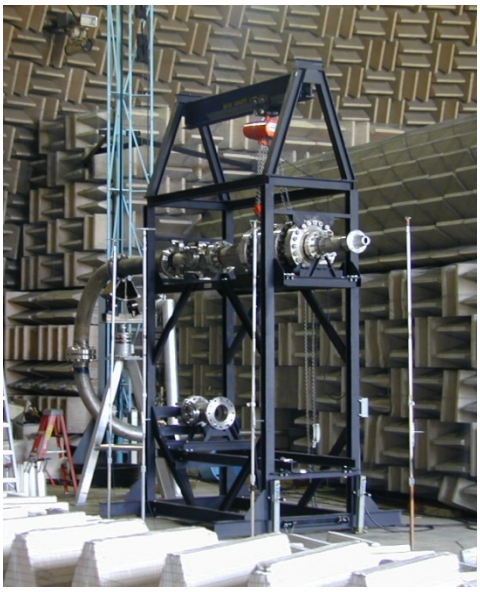

Figure 7.—Photograph of the SHJAR.

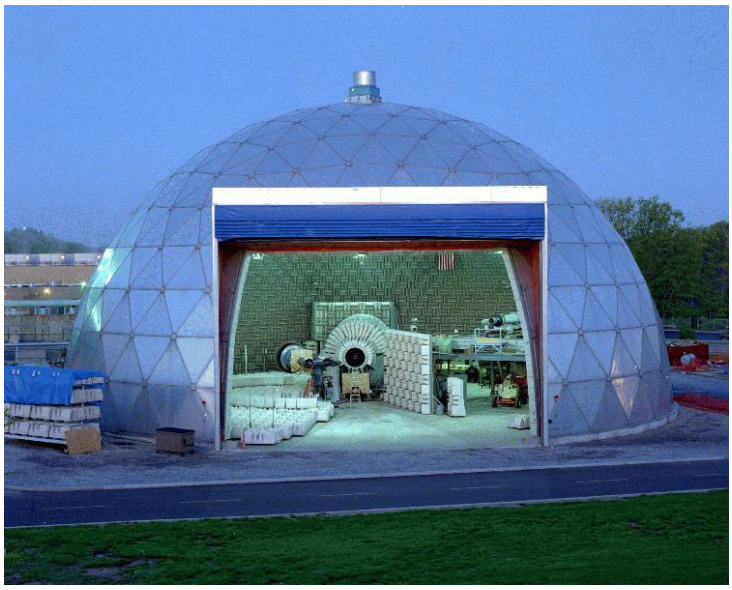

Figure 8.—Photograph of the AAPL laboratory. SHJAR is assembly the smaller rig left of center.

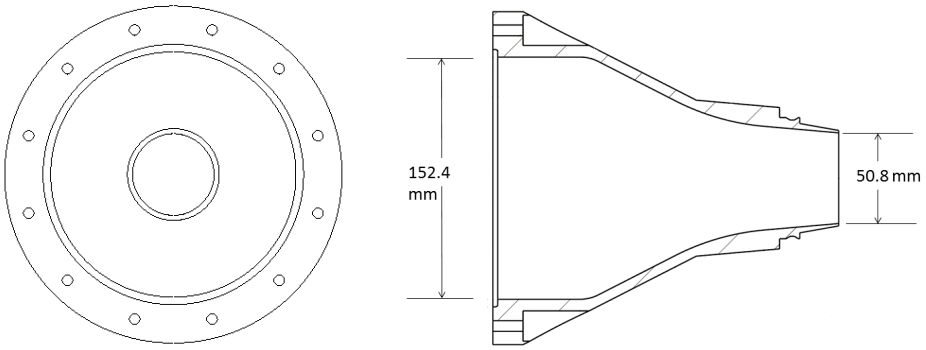

Figure 9.—SHJAR baseline SMC000 nozzle.

sound absorbing wedges providing a near anechoic environment. The centerline nozzle exit of the SHJAR is 3 m above of the floor. Vitiated flow heating up to 830 K is provided by an inline hydrogen combustor and supply air is provided by central compressor facilities, permitting continuous operation. The fuel-air mass flow ratios for heating the supply air ranged from 2.8×10^{-4} to 7.2×10^{-3} resulting in a negligible change in the nitrogen to oxygen ratio at the nozzle exit.

The SHJAR facility is frequently used for PIV measurement studies where aluminum oxide is used to seed the flow. Raman scattering is a molecular scattering technique and as such any particulates in the flow are detrimental to the quality of the acquired Raman signals, hence, in preparation for the test, the SHJAR was disassembled and cleaned of any residual seed material coating the inside flow passages of the rig/model hardware. As an extra precaution the supply air was filtered to eliminate any residual particulate matter entrained in the flow. For this test a single nozzle, denoted as SMC000, was installed on the SHJAR. The SMC000, is a baseline axisymmetric nozzle with an exit diameter of 50.8 mm and a throat area of 3.142 in.^{2} (Fig. 9).

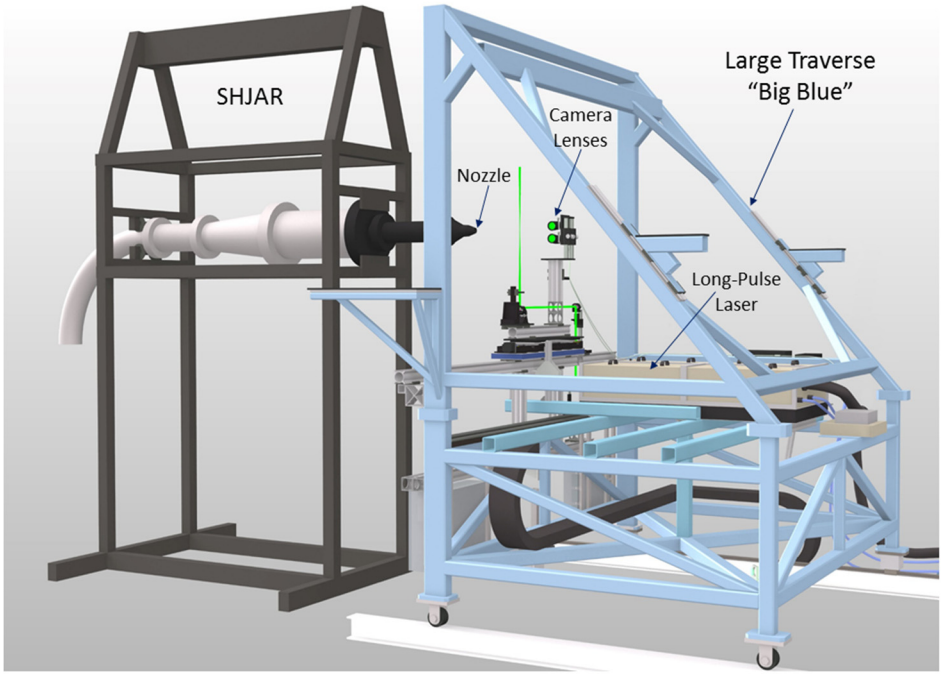

Figure 10.—SHJAR and large traverse "Big Blue" loaded with the long-pulse laser and optical diagnostics.

The same optical excitation and detection system used to acquire the laboratory calibration was also used in the performance of actual testing in the AAPL. The long-pulse, Agilite laser, beam insertion optics, detection optics and spectrometer/camera detection systems were transported, installed, and aligned in the AAPL as shown in Figure 10. The Agilite laser was mounted inside the frame of the large traverse system, affectionately called "Big-Blue". The beam from the laser was directed towards the front face of Big-Blue where it was turned vertical using a mirror. A catching mirror then turned the laser beam horizontal and parallel to the front face of Big-Blue. A final turning mirror turned the laser beam vertical so that it passes vertically through the jet flow field. A 500 mm focal length spherical lens then focused the beam at the center of the flow, downstream of the nozzle's exit plane. The final turning mirror, lens and the camera collection lenses are mounted on a long Velmex traverse stage which provides the radial surveys of the jet plume.

Since Raman spectroscopy is a point measurement diagnostic, it requires a translation of the excitation and detection optics in both the axial and radial directions in order to provide a survey of the jet plume temperature field. The data obtained in the AAPL were acquired over a grid of measurement locations for nine experimental setpoints that covered a wide range of flow conditions. As stated previously, the measurement grid was developed by using the PIV Consensus data acquired with the same experimental rig configuration. The grid was divided into three regions: (1) centerline scans (running downstream along the centerline of the jet); (2) a lip line scan (running downstream at the nozzle lip line); and (3) a series of radial scans at axial stations of x/D_j = 2, 4, 8, 12, and 20. A total of 63 measurement locations were acquired at each rig operating point, which consumed a complete 6 hr test run. A plot showing the measurement grid for setpoint 7 is shown in Figure 11.

The grid points in the figure are overdrawn on top of a previously measured velocity field at setpoint 7 in order to better show the reasoning behind the selection criteria for the measurement locations. At the beginning of a run day, background image spectra were recorded to provide a background spectra for baseline removal. Additionally, Rayleigh line spectra were acquired each run day for characterization of the instrument function. At each measurement station, 1000 single shot spectra were recorded.

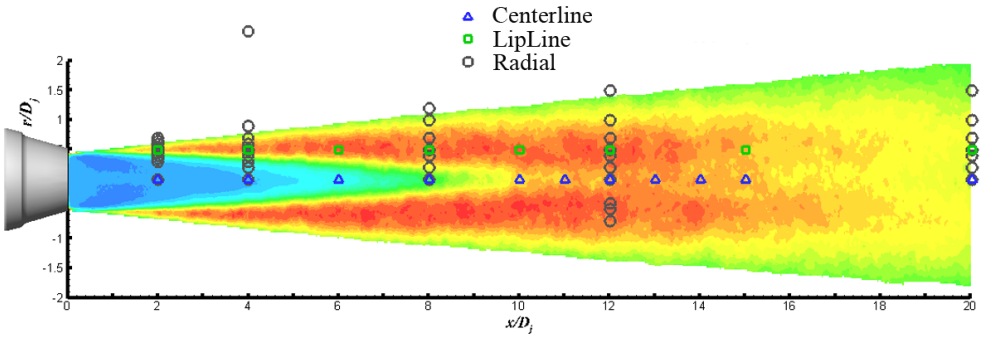

Figure 11.—Rotational Raman measurement grid for setpoint 7.

Consensus Velocity Database

As stated earlier, the Raman temperature diagnostic was to be applied in the SHJAR facility on the SMC000 nozzle in order to provide a set of temperature measurements to complement the large database of velocity measurements that have been collected on both hot and cold jet flows that comprise the "Consensus" data set. Details describing the development of the consensus data set are provided in the previously mentioned reference by Bridges and Wernet (Ref. 12). Essentially two similar jet nozzle flows have been measured many different times (> 30) over a period of 15 years using a wide variety of different camera sensor resolutions, with both large and small fields of view, in various configurations of 2-component PIV, Stereo PIV and Temporally-Resolved PIV. This voluminous collection of PIV data on both hot and cold jets has been compared with historical jet flow measurements (hotwire and LDV) and used to build a consensus data set that brackets the expected flow velocities and turbulence intensities that one would expect to measure in one of these jets at the list of operating conditions tabulated in that report. The data are publicly available on a NASA Langley's CFD code validation case web site listed in Bridges and Wernet (Ref. 12).

In this current work, the consensus data set is invoked to provide a well-established velocity magnitude and turbulence intensity reference at an M 0.9 flow condition, across three different temperature ratios: setpoints 7, 27, and 46. The consensus PIV measurements presented here characterize the momentum transfer properties of these hot and cold jet flows, which indoctrinates the reader for the presentation of the temperature measurements in these same flow fields. The database provides the bracketed range within which one would expect high quality, high accuracy PIV measurement results to fall. While the mean velocity and turbulence intensity profiles along with their bracketed error bars are available in the consensus data set, here we chose just to show the mean trends without error bars.

In Figure 12 the centerline ($r/D_j = 0$) velocity profiles and turbulence intensities for setpoints 7, 27, and 46 are plotted. The left vertical axis is the normalized axial velocity (U/U_j) and the right vertical axis is the axial turbulence intensity (u'/U_j). The turbulence intensities are defined as the rms velocity normalized by the axial component of the jet exit velocity. The cold jet case of setpoint 7 shows a relatively long potential core lasting out to approximately 12 x/D_j. The centerline turbulence levels peak when the two shear layers on each side of the jet merge together, which for this cold jet case are relatively low at 13 percent. As the heat is increased and the Mach number remains the same, the length of the potential core decreases down to approximately 10 x/D_j for the setpoint 27 and 46 cases. The turbulence levels are also observed to increase as the temperature in the jet increases up to roughly 15 percent.

Similarly, the resultant lip line plots ($r/D_j = 0.5$) for setpoints 7, 27, and 46 are presented in Figure 13, where a general steady decay in the velocity magnitude is observed, which is again normalized by the axial component of the jet exit velocity. In the cold jet case, setpoint 7, the velocity has an initially higher velocity magnitude than the heated jet cases. The turbulence in the shear layer is observed to peak at approximately $x/D_j = 10$ for the cold jet case, whereas in the hot jet cases the peak turbulence is very close to the start of the shear layer near the nozzle exit. The peak turbulence levels are observed in the highest jet temperature case of setpoint 46.

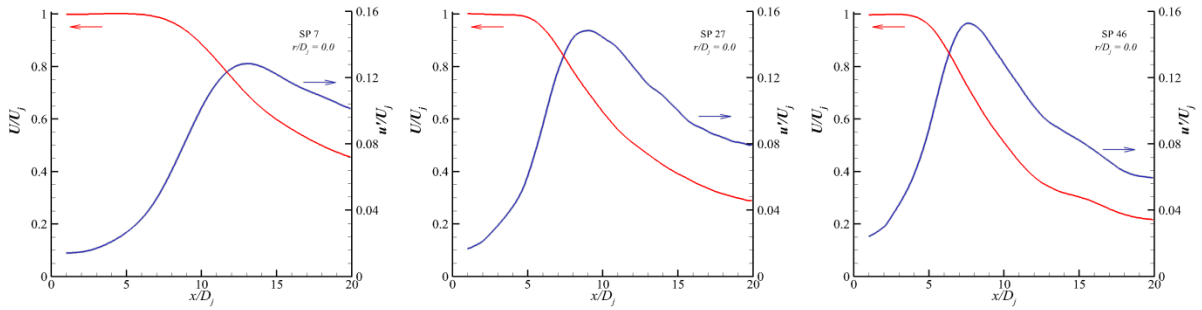

Figure 12.—Centerline plots of normalized axial velocity (U/U_j) (in red along left axis) and axial turbulence intensity (u'/U_j) (in blue along right axis) for setpoints 7 (left), 27 (middle), and 46 (right).

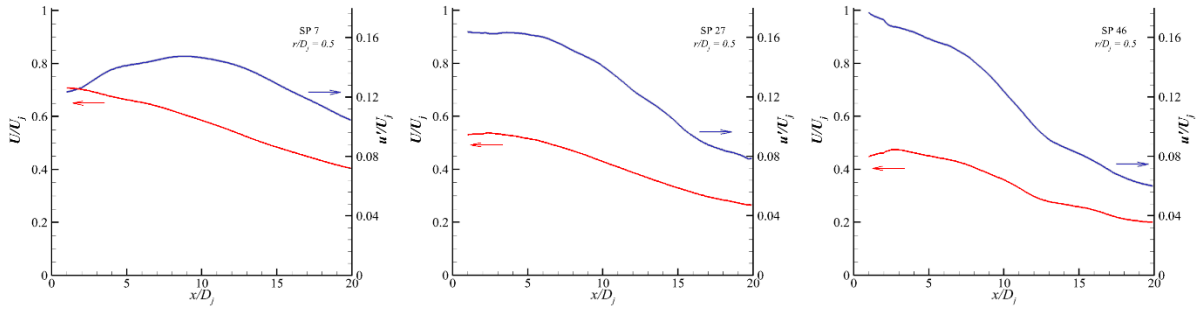

Figure 13.—Lip line plots of normalized axial velocity (U/U_j) (in red along left axis) and axial turbulence intensity (u'/U_j) (in blue along right axis) for setpoints 7 (left), 27 (middle), and 46 (right).

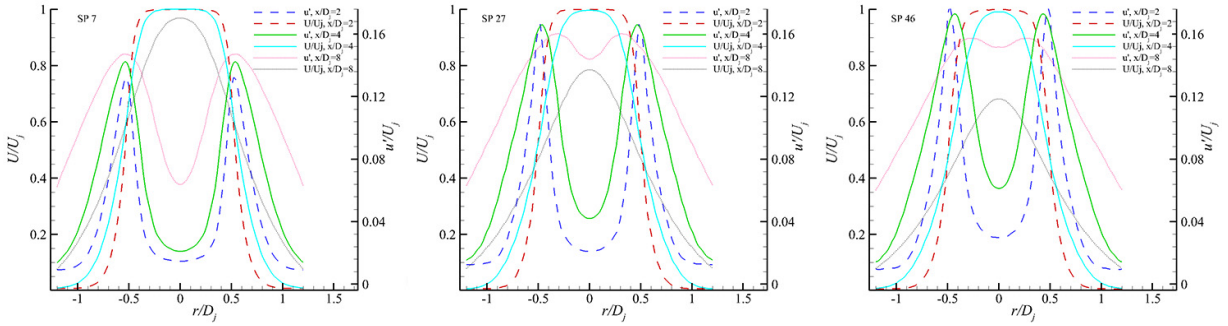

Figure 14.—Radial plots of normalized axial velocity (U/U_j) (left axis) and axial turbulence intensity (u'/U_j) (right axis) at x/D_j = 2 (dashed lines), 4 (solid lines), and 8 (dotted lines), downstream of the nozzle exit plane.

The radial line plots in Figure 14 show cross sectional views of the information contained in the centerline and lip line plots. Three different cross-stream slices through the flow are shown: x/D_j = 2, 4, and 8. The additional information gained from the radial profiles is the definition of the initial width of the jet core and the narrowing of the potential core with increasing x/D_j. The shear layers (centered at $r/D_j = \pm 0.5$) are very narrow close to the nozzle exit and decrease in magnitude as they spread out with increasing distance downstream. The profiles at x/D_j = 8 clearly show that the potential core has not ended for the cold jet case (denoted by the deep valley in the turbulence level at the centerline of the jet) and are nearly ended for the hot jet cases. Hence, the cold jet has a long potential core that ends at approximately x/D_j = 12, while the heated jet cases exhibit progressively shorter potential cores with increasing temperature.

TABLE 1.—TEST MATRIX OF SETPOINTS/RIG CONDITIONS

Setpoint	Temperature (K)	Ma	T_j/T_∞	NPR	NTR	ṁ[lb/s]
7	245	0.9	0.835	1.86	0.997	1.93
23	519	0.5	1.765	1.103	1.81	0.233
27	519	0.9	1.765	1.36	1.92	0.419
29	519	1.33	1.765	1.898	2.109	0.619
32	668	0.5	2.27	1.079	2.317	0.182
36	668	0.9	2.27	1.274	2.423	0.327
38	668	1.33	2.27	1.663	2.604	1.08
46	795	0.9	2.7	1.227	2.848	0.276
49	795	1.48	2.7	1.698	3.101	0.453

Results and Discussion

Temperature data were acquired over a wide range of flow temperatures and Mach numbers as listed in Table 1. In this work, only results for three of these conditions will be presented: setpoints 7, 27, and 46, which are all at Mach 0.9, but at temperature ratios of 0.84, 1.77, and 2.7. Three different Raman thermometry measurement surveys were performed for each setpoint. Centerline profiles ($r/D_j = 0$), lip line profiles ($r/D_j = 0.5$), and a series of radial profiles at $x/D_j = 2, 4, 8, 12, 20$. The data collected at setpoint 7 were spaced closer together further downstream than the surveys performed at all of the other hot setpoints, where the potential core length of the jet is presumed to shorten due to the heated flow. For each radial survey an ambient temperature point was acquired ($x/D_j = 4$, $r/D_j = 2.5$) using the Raman measurement system. These ambient temperatures and their rms temperature variations provide a check on the performance of the Raman measurements in the jet flow facility, where the acoustic noise levels exceed 115 dB. The ambient temperatures were within a few degrees (2 percent) of the ambient temperatures recorded using the SHJAR facility thermocouples mounted at the jet exit height in the facility. The rms temperature variations of the ambient temperature measured using the Raman thermometry system were < 3 percent. Hence, the Raman diagnostic system installed in the SHJAR was able to produce accurate temperature measurements (while the rig was running), with < 3 percent rms levels in the quiescent ambient air. Any measurements in the jet flow will have this inherent measurement variation σ_{RE} given by Equation (4) added with the rms temperature variations in the jet flow.

The temperature data are nondimensionalized by subtracting the ambient temperature T_∞ and dividing by the difference between the jet exit temperature T_j and the ambient temperature. Referencing the temperature data to the ambient temperature puts the data in a similar frame of reference as the velocity data where the ambient velocity, $U_\infty = 0$. Technically, the velocity data should be defined as $u'/(U_j-U_\infty)$, but for brevity we omit U_∞. For the case of setpoint 7, the jet exit temperature is below the ambient temperature, hence the numerator difference is reversed so that the normalized temperature yields a positive result. For the plots of the normalized rms temperature, the standard deviation in temperature T' is normalized by the difference between the jet exit temperature and the ambient temperature $\Delta T = T_j-T_\infty$.

The consensus PIV data set illustrated that the turbulence level on the jet centerline near the nozzle exit for these hot and cold jet flows is between 1 to 3 percent, as shown in Figure 12. The Raman thermometry diagnostic system has an inherent measurement variation, as demonstrated in the lab scale calibration. The lab scale calibration data, which was performed in an isothermal heat gun flow, is assumed to be free from turbulent temperature variations, and represents only the rms variation in the Raman thermometry technique as a function of temperature. If we assume that the inherent Raman measurement σ_{RE} error is added in quadrature with the normalized rms variations in temperature of the flow, σ_{TI}, then the actual measured variation in flow temperature σ_m can be approximated by:

$$\sigma_m^2 = \sigma_{TI}^2 + \sigma_{RE}^2 \tag{5}$$

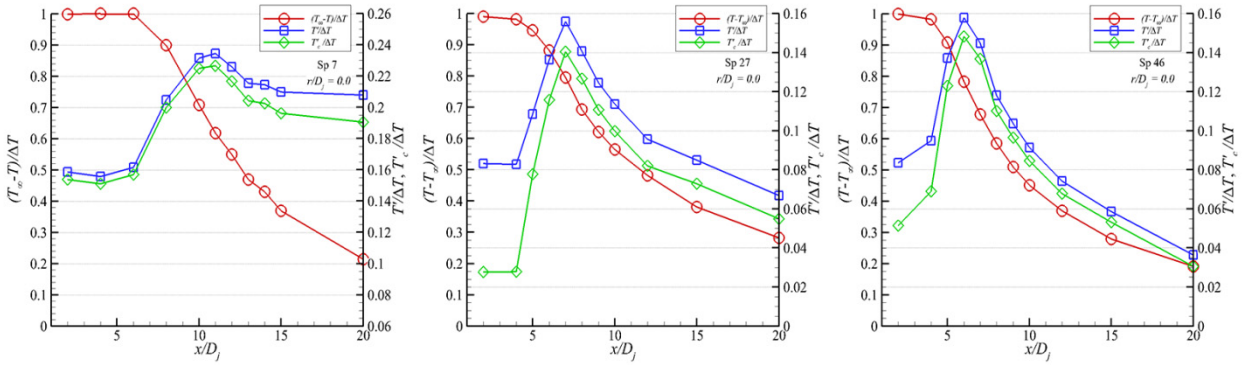

Figure 15.—The normalized centerline temperature plotted in red circles (left axis), the normalized rms temperature is plotted in blue squares (right axis) and the corrected normalized rms temperature is plotted in green diamonds (right axis) for each setpoint: 7 (left), 27 (middle), and 46 (right).

The effect of removing the inherent rms is illustrated for measurements near the jet exit, on the nozzle centerline. For the centerline survey measurements in the jet at $x/D_j = 2$, rms variations in temperatures were observed on the order of 7 K at setpoint 7, 18 K at setpoint 27 and 40 K at setpoint 46. From the lab scale calibration data (Eq. (1)), the estimated rms variations are 2, 16.5, and 31.4 K, at the jet exit temperatures of 240, 500, and 760 K, respectively. Rearranging Equation (5) and solving for σ_{TI}, the rms variations in flow temperature on the jet core centerline are computed to be 6.2 K, at 240 K, 7.4 K at 500 K and 17.6 K at 760 K, respectively. When normalized by their respective ΔT's, the normalized rms variations in temperature are: 14, 3.2, and 5 percent, respectively.

Figure 15 shows the normalized centerline temperatures plotted using red circles on the left axis, the normalized rms temperature is plotted in blue squares on the right axis and the corrected normalized rms variations in temperature ($T'_c/\Delta T$) are plotted in green diamonds on the right axis for setpoints Sp7 (left), Sp27 (middle), Sp46 (right). Generally the σ_{RE} correction has more effect in the high temperature regions of the flow. Hence for the hot jet cases the correction is highest on the nozzle centerline, while for the cold jet flow the correction (albeit minimal) is larger in the warmer ambient regions of the flow. The setpoint 7 centerline temperature profile shows a long thermal potential core in agreement with the observed momentum field potential core length of approximately $x/D_j = 12$. The normalized rms temperature plot shows a moderate level of turbulence in the jet core which peaks at $T'/\Delta T = 23$ percent at approximately $x/D_j = 12$ and then begins to slowly decay.

The rms variations in temperature for the setpoint 7 data are very small due to the low temperatures in the jet relative to the ambient room temperature air, which are even lower than the inherent rms variations in the Raman thermometry technique at the jet exit temperatures. In order to have the expected 1 percent normalized rms in the jet exit temperatures for setpoint 7, the measured rms values would have to be on the order of 4 K, which is below the demonstrated inherent rms variation of the Raman thermometry diagnostic as configured for this experiment. The measured normalized rms variations in temperature at the jet exit for setpoint 7 are much larger than expected since we have reached the noise floor of the technique for these cold flows. However, the location of the peak rms variations in the jet flow are still readily apparent in the data and clearly delineate the axial location of the peak.

At setpoint 27, the centerline temperature profile decays much sooner at approximately $x/D_j = 7$. The corrected normalized rms temperature starts out low in the jet core (2.5 percent) and is observed to peak at 14 percent at approximately $x/D_j = 7$ and then decays with increasing distance downstream. At setpoint 46, the centerline temperature profile decays very quickly following the trend of the decreasing potential core length with temperature. The corrected, centerline normalized rms temperature starts out at about 5 percent in the jet core and reaches a peak of 15 percent at approximately $x/D_j = 6$ followed by again an even faster decay down to a lower final normalized rms temperature at $x/D_j = 20$ than was observed at setpoint 27. Generally, the centerline behavior of the normalized temperature profiles and corrected

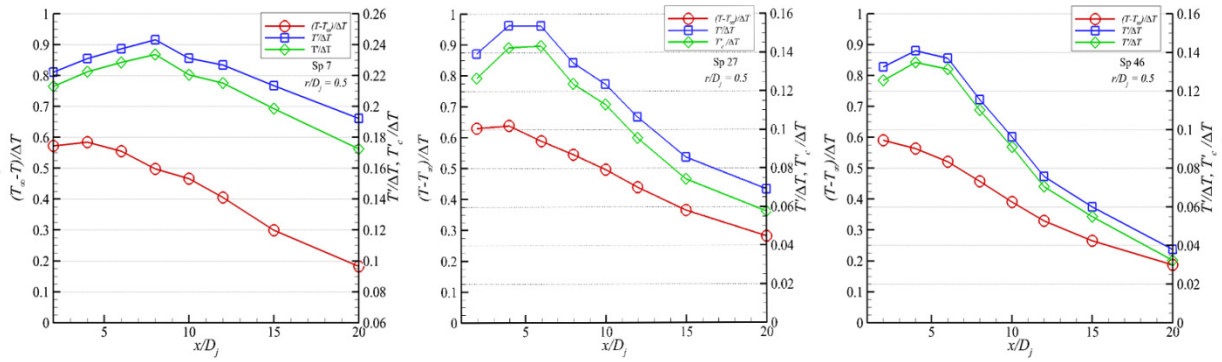

Figure 16.—The normalized lip line temperatures are plotted in red circles (left axis), the normalized rms temperatures are plotted in blue squares (right axis) and the corrected normalized rms temperatures are plotted in green diamonds (right axis) for each setpoint: 7 (left), 27 (middle), and 46 (right).

normalized rms temperature in the heated jet cases closely mirrors the observed trends in the centerline velocity profiles and turbulence intensities in Figure 12. However, the rms temperature peaks a little sooner and decays faster than the centerline flow turbulence.

The normalized rms fluctuations in temperature in the jet core are not as low as in the PIV data, nor do they show the same maximum values. The Raman thermometry data may suffer from a small amount of low pass filtering of the turbulent temperature fluctuations in the flow. Recall that the Raman thermometry diagnostic probe volume is 70 µm in diameter and 6 mm long. The long axis of the probe volume is oriented vertically and the surveys of the jet plumes were performed in the transverse direction. Hence, the Raman system was sensitive to the radial gradients in the flow since this was the 70 µm axis of the probe volume. There was however, some degree of spatial averaging along the 6 mm length of the probe volume. Fortunately, the 6 mm vertical probe volume length samples a relatively uniform portion of the flow at the 25 mm radius of the jet shear layer, i.e., there is little curvature of the flow features across the probe volume, which was scanned across the horizontal centerline of the jet flow. However, the extended length of the probe volume does yield a small amount of spatial averaging, which results in a slight under prediction of the peak rms fluctuations in the gas temperature. Planned future measurements in the SHJAR will focus on using longer focal length collection lenses in order to reduce the imaged length of the probe volume.

Figure 16 shows the normalized lip line temperatures plotted in red circles on the left axis, the raw normalized rms temperature plotted in blue squares on the right axis and the corrected, normalized rms temperature plotted in green diamonds on the right axis for setpoints Sp7 (left), Sp27 (middle), Sp46 (right). The normalized temperature profile behavior and the normalized rms temperature are very similar to the momentum mean flow and fluctuation behavior along the lip line. The peak normalized rms temperature is near the nozzle exit followed by a slow decay. The cold jet case normalized rms variations in temperature are higher than the momentum turbulence levels, again due to the fluctuation levels in the cold flow case being below the sensitive range of the technique.

For setpoint 46, the normalized rms temperature peaked at about 75 K, for setpoint 27 peak rms levels of 33 K were measured and for setpoint 7, the peak rms temperature was measured at 10.5 K. While the magnitude of the normalized rms temperature levels in the cold jet case are higher than the turbulence levels shown in Figure 12, the general shape of the profile is very similar.

In Figure 17 the radial profiles through the shear layer are plotted for the three different setpoint cases, at three different axial stations: x/D_j = 2, 4, and 8. Again both the raw and corrected normalized rms temperature are plotted. For setpoint 7, at x/D_j = 2 the temperature profile starts to decay from the relatively flat jet core temperature at an r/D_j = 0.5. The normalized rms temperature in the jet core are, as already described, higher than the momentum cases. However, the normalized rms temperature still exhibits a clear peak at r/D_j = 0.7. The shear layer is occurring at a larger radius than anticipated, hence the complete profile of the shear layer is not resolved. At x/D_j = 4, the radius of the jet core has shrunk and the decay down to the ambient temperature is slower. Again, it appears that the radial extent of the

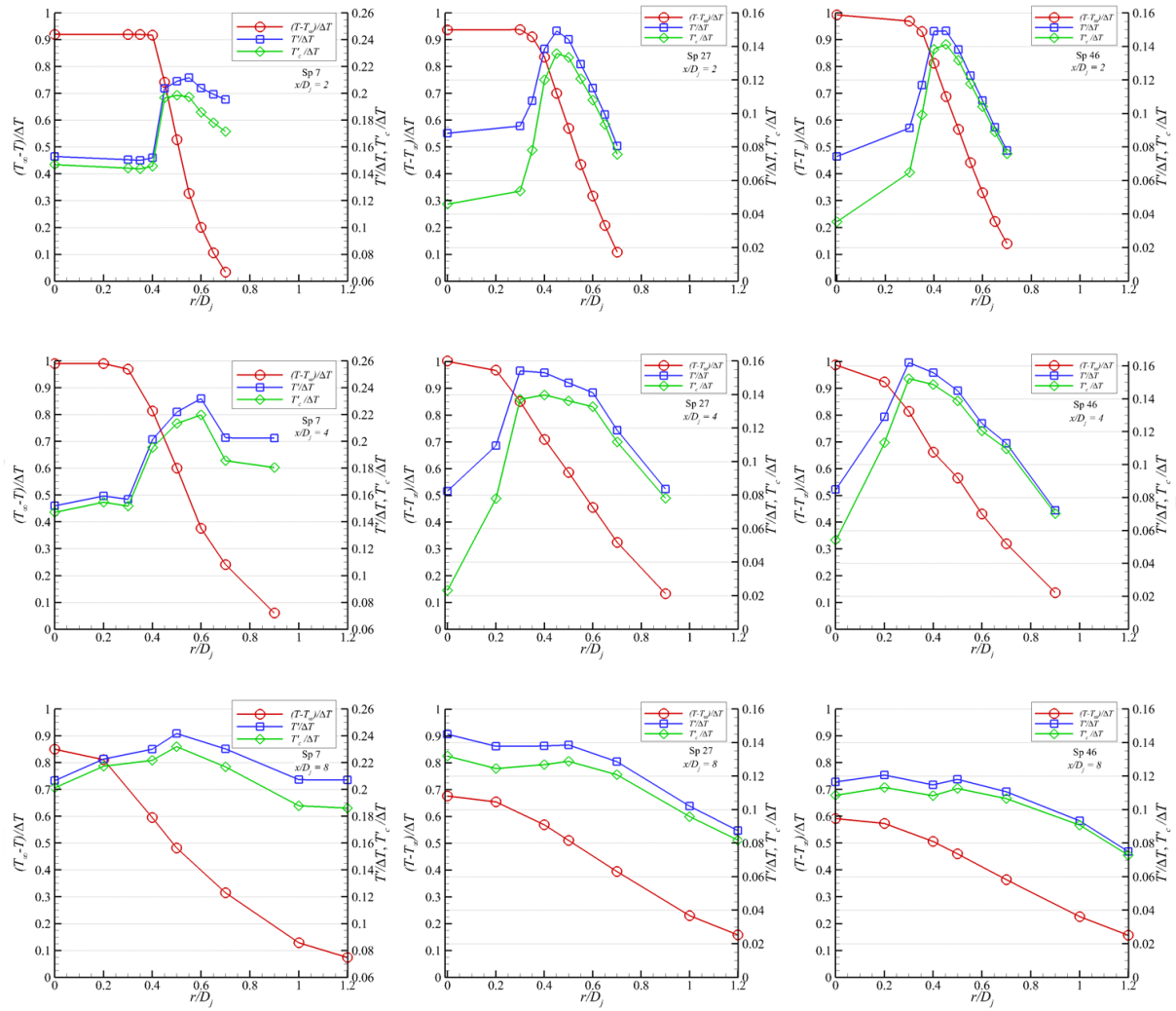

Figure 17.—Plots of the radial profiles through the shear layer are shown plotted in red circles (left axis), the normalized rms temperatures are plotted in blue squares (right axis) and the corrected normalized rms temperatures are plotted in green diamonds (right axis) for each setpoint: 7 (left), 27 (middle), and 46 right) at three different axial stations x/D_j = 2 (top), 4 (middle), and 8 (bottom).

survey was insufficient to define the outside edge of the thermal shear layer, which still may be difficult to discern due to the relatively small ΔT between the jet core and the ambient. The shear layer is much broader but still at about the same value of $r/D_j = 0.7$. At $x/D_j = 8$, the normalized temperature profile exhibits a continuous decay from the jet centerline and the peak value is below the core jet temperature. The shear layer is very broad at this location, but there is still a small dip on the jet core, indicating that the potential core of the jet has not yet been reached.

For the setpoint 27 radial profiles at $x/D_j = 2$, the jet core temperature profile drops from the flat jet core exit temperature down towards the ambient temperature beginning at $r/D_j = 0.4$. The temperature shear layer is well defined with a peak normalized rms temperature occurring at approximately $r/D_j = 0.45$. At $x/D_j = 4$, the thermal core of the jet has decreased in radius and the shear layer normalized rms temperature is wider, and peaks closer to the centerline at $r/D_j = 0.3$. At $x/D_j = 8$, the normalized temperature profile is very broadly shaped and the shear layer is a broad function slowly decaying from the jet centerline normalized rms temperature, confirming that the potential core of the jet has been reached. For the setpoint 46 radial profiles in the figure, the details of the radial profiles are nearly identical to those observed at setpoint 27. The only exceptions being that the normalized rms temperatures are slightly higher, and the temperature shear layer is slightly thinner.

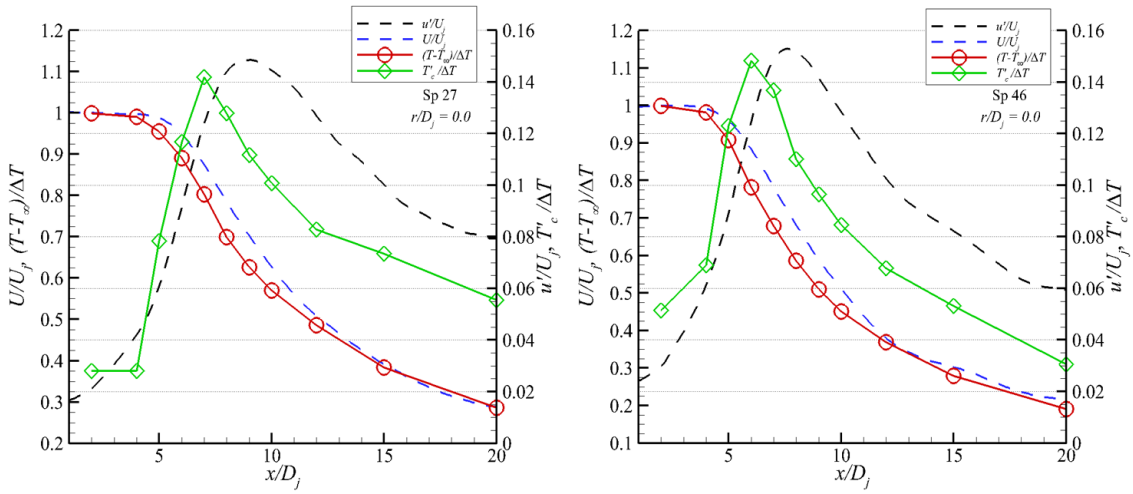

Figure 18.—Comparison of the centerline momentum decay to temperature decay for the hot jet cases. The consensus velocity data are shown in the dashed lines and the thermal profile and corrected normalized rms temperature are plotted as lines with symbols.

The decay of the centerline temperature and velocity are governed by the heat transfer and turbulent mixing of the jet with the ambient air. A comparison of the consensus centerline velocity and turbulence intensity with the normalized thermal profile and normalized rms temperature for the hot jet cases (Sp 27 and Sp 46) are shown in Figure 18. There are two notable features in these comparison plots. First, the thermal profile appears to decay slightly earlier, but at essentially the same rate as the normalized velocity profile.

The temperature decay appears to be coupled with the velocity decay, which is driven by the mixing of the hot jet core flow with the cooler ambient air. Secondly, although the magnitude of the normalized rms temperature is nearly identical to the axial turbulence intensity, the rms temperature peaks earlier and then decays faster than the flow turbulence. The magnitude of the temperature fluctuations is decreasing faster in the downstream direction due to the smaller local difference in temperatures of the thermal eddies, as defined by the thermal profile. Hence, while the temperature decay appears to be coupled with the velocity decay, the rms temperature indicates the packets of hot fluid are being dissipated faster than the momentum of the flow, which agrees with the general assumption that the thermal dissipation occurs faster than the momentum dissipation in turbulent flows (Prandtl# < 1) (Ref. 20). In fact the ratio of the rms temperature to rms velocity as shown in Figure 18, is nominally 0.7 in the fully mixed turbulent region of the jet flow, $x/D_j > 10$.

Finally the complete temperature mapping fields for each setpoint are shown in Figure 19, where the results of the centerline, lip line and radial profiles (63 points) are all combined into a single scatter plot. The unique marker shapes for the three different surveys are shown in the plot legend. The symbols are colored by the mean flow temperature measured at each location. Note the vertical scale has been expanded to enhance the legibility of the plot.

Many of the lip line and centerline measurement points overlap the radial profile points. When all of the data are plotted on the scatter plot, the temperatures from two different surveys do not always agree at the same measurement point. The three different surveys for each rig setpoint were acquired at different times (the entire 63 grid required 6 hr of runtime). The high air mass flow, high pressure heated stream required to maintain the operating points in the SHJAR is provided by central services. During these long duration runs, variations in the facility air supply can occur due to other large facilities at the lab coming on-line or going off line during our test runs. Hence, while the rig operator endeavors to keep the rig on the desired operating point, some variation off of the rig operating point is not uncommon. These variations are confirmed with rig instrumentation reading recorded at the beginning of each Raman temperature measurement acquisition. The scatter plots shows the concentration of measurements across

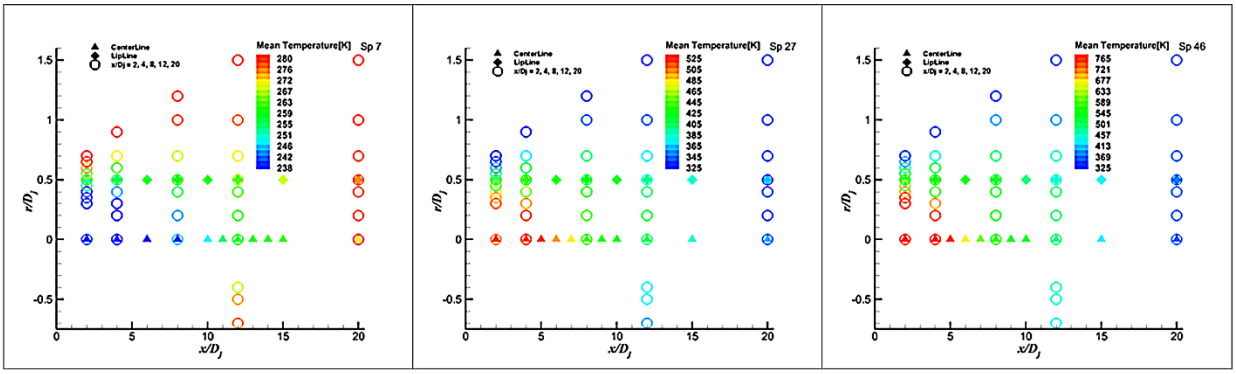

Figure 19.—Temperature scatterplots for setpoints 7, 27, and 46 showing the Raman-derived temperature for the nozzle centerline (▲, r/D_j = 0.0), nozzle lip line (♦, r/D_j = 0.5) and all radial points (○).

the shear layer and along the nozzle centerline. Some measurements are obtained on the $r/D_j < 0$ side of the jet at $x/D_j = 12$ to check/confirm the symmetry of the jet. When plotting the mean flow temperature instead of the normalized flow temperature for the cold jet flow case we see that the core flow is actually below the ambient temperature due to the isentropic expansion cooling of the jet flow through the nozzle into the ambient air.

Conclusions

The first ever application of rotational Raman temperature measurements in heated turbulent, high-velocity flows have been reported. We believe that these are the most comprehensive, high quality set of temperature measurements ever obtained in hot and cold nozzle flows. They were performed with a great degree of spatial resolution and with higher accuracy than that obtained by previous techniques. The data demonstrated rms errors down to < 3 percent in quiescent air at room temperature. An inherent measurement error (caused by thermal motion of the molecules) was demonstrated to be linear with temperature. A correction of the inherent rms variations in the Raman based temperature measurements was applied to the data. A comparison of the temperature data with the previously acquired PIV consensus dataset was performed which showed that many of the trends in the turbulence and velocity field decay were also observed in the normalized rms temperature and normalized temperature profiles measured using the new Raman based diagnostic. Normalized temperature profiles were readily resolved for all of the setpoint cases presented. It was difficult to resolve the small scale rms temperature in the cold jet flow, since these levels were below the measurement noise floor of the Raman diagnostic; however the shear layer peaks and extent were still resolved. For the heated jet flow cases, the measured normalized rms temperatures had similar peak levels and peak locations as the flow turbulence levels measured previously using PIV. These data confirm for the first time that the spatial extent and nominal normalized rms variations in the hot and cold jet flows mirror the momentum field properties, an assumption that has been invoked for many years by CFD modelers. The most notable exception is that for the hot jet centerline cases the rms temperature peaked earlier and decayed faster than the turbulence intensity, confirming the general assumption that the thermal dissipation occurs faster than the momentum dissipation in turbulent flows (Pr < 1). The results obtained in the AAPL have demonstrated that this technique should be applicable in other flow fields of interest, even in some combusting environments such as propane, natural gas fire heaters, to name a few.

Future Work

A more detailed examination and comparison of all of the temperature data acquired during this test with the corresponding benchmark velocity measurements acquired previously for the same nozzle will be conducted in a future publication. Additionally, a similar comparison will also be undertaken with Rayleigh temperature measurements previously acquired in AAPL. The length of the Raman thermometry diagnostic

probe volume has been reduced to less than 2 mm in length using different collection lenses, with no reduction in the signal levels. Additional reductions in the probe volume length are planned through the use of cladding free fibers in the fiber-optic imaging bundle used to collect the signal. Improvements in the data acquisition process have already been made with the acquisition of the latest PI-MAX4 ICCD camera and Lightfield® (Roper Scientific, Inc.) software. The new camera's high quantum efficiency will increase the Raman signal gathering capability and the simultaneous acquisition feature of both accumulated and single-shot spectra will shorten the data acquisition time significantly. Further experiments in the AAPL for the acquisition of Raman temperature measurements are also in preparation. These tests will examine flows from nozzles that are much more complex than the simple model used in the current study and will aid in the design of new nozzle platforms/configurations as well as continuing to support NASA's validation of physics-based CFD codes efforts.

References

1. Laurence, J.C. 1956 Intensity, Scale, and Spectra of Turbulence in Mixing Regions of Free Subsonic Jet, *NACA Report* 1292.
2. Lau, J.C., Morris, P.J. and Fisher, M.J. 1979 Measurements in Subsonic and Supersonic Free Jets Using a Laser Velocimeter, *J. Fluid Mech.* 93:1 1-27.
3. Bridges, J. and Wernet, M.P. 2003 Measurements of the Aeroacoustic Sound Source in Hot Jets, *AIAA Paper* No. 2003-3130.
4. Panda, J., Seasholtz, R.G., Elam, K.A. 2005 Investigation of Noise Sources in High-Speed Jets Via Correlation Measurements, *J. Fluid Mechanics*, 537 349-385.
5. Mielke, Amy F., Elam, Kristie A. 2009 Dynamic Measurement of Temperature, Velocity, and Density in Hot Jets Using Rayleigh Scattering, *Experiments in Fluids*, 47:6 673-688.
6. Cutler, A.D., Danehy, P.M., Springer, R.R., O'Byrne, S., Capriotti, D.P. and Deloach, R. 2003 Coherent Anti-Stokes Raman Spectroscopic Thermometry in a Supersonic Combustor, *AIAA Journal*, 41:12 2451-2459.
7. Woodmansee, M.A., Iyer, V., Dutton, J.C., and Lucht, R.P. 2004 Nonintrusive Pressure and Temperature Measurements in an Underexpanded Sonic Jet Flowfield, *AIAA Journal*, 42 6.
8. Kuehner, Joel P., Tessier, Andrew F., Kisoma, Allan, Flittner, Jonathan G., McErlean, Michael R. 2010 Measurements of Mean and Fluctuating Temperature in an Underexpanded Jet Using Electrostrictive Laser-Induced Gratings, *Experiments in Fluids* 48 421-430.
9. Ajrouche, H., Lo, A., Vervisch, P., and Cessou, A. 2014 1D Single-Shot Thermometry in Flames by Spontaneous Raman Scattering Through a Fast Electro-Optical Shutter, 17th International Symposium on Applications of Laser Techniques to Fluid Mechanics, Lisbon, Portugal.
10. Lee, T., Bessler, W., Kronemayer, H, Schulz, C, and Jeffries J. 2005 Quantitative Temperature Measurements in High-Pressure Flames with Multiline NO-LIF Thermometry, *Appl Opt*. 44:31 6718-28.
11. Thurber, M.C. and Hanson, R.K. 2001 Simultaneous Imaging of Temperature and Mole Fraction Using Acetone Planar Laser-Induced Fluorescence, *Experiments in Fluids* 30:1.
12. Bridges, J. and Wernet, Mark P. 2011 "The NASA Subsonic Jet Particle Image Velocimetry (PIV) Dataset," NASA Technical Memorandum, NASA/TM—2011-216807.
13. Ferraro, J.R., and Nakamoto, K. 1994 *Introduction to Raman Spectroscopy*, Academic Press, San Diego, CA.
14. Eckbreth, A.C. 1988 *Laser Diagnostics for Combustion Temperature and Species*, Abacus Press, Cambridge, MS.
15. Coney, T.S., 1971 Determination of the Temperature of Gas Mixtures by Using Laser Raman Scattering, Cleveland Ohio, NASA-TN-D-7126.
16. Fedorov, S. 2013 "Ratio of Rotational Raman Cross Sections for Oxygen and Nitrogen Measured in Air," *Atmospheric and Oceanic Optics*, 26:1 5-7.
17. Laher, R.R. 1991 "Improved Fits for the Vibrational and Rotational Constants of Many States of Nitrogen and Oxygen," *Journal of Physical and Chemical Reference Data*, 20:4 685-712.

18. Hoskins, L.C. 1975 Pure Rotational Raman Spectroscopy of Diatomic Molecules, *Journal of Chemical Education*, 52:9 568-572.
19. James, T.K. 1959 Line Intensities in the Raman Effect of 1Σ Diatomic Molecules, *Journal of Chemical Physics* 31:1,130-134.
20. Bolin, Alexis, 2008 *Investigation of high Resolution Vibrational CARS Thermometry*, Master's Thesis, Lund University, Sweden.
21. Kays, W.M. and Crawford, M.E., 1993, *Convective Heat and Mass Transfer*, McGraw-Hill, New York, 3rd ed.